

Live-cell painting: Image-based profiling in live cells using acridine orange

Fernanda Garcia-Fossa^{a,b}, Thaís Moraes-Lacerda^a, Mariana Rodrigues-da-Silva^a, Barbara Diaz-Rohrer^b, Shantanu Singh^b, Anne E. Carpenter^b, Beth A. Cimini^b, and Marcelo Bispo de Jesus^{b,a,*}

^aDepartamento de Bioquímica e Biologia Tecidual, Instituto de Biologia CP 6109, Universidade Estadual de Campinas (UNICAMP) 13083-970, Campinas, SP, Brasil; ^bImaging Platform, Broad Institute of MIT and Harvard, Cambridge, MA 02142

ABSTRACT Image-based profiling has been used to analyze cell health, drug mechanism of action, CRISPR-edited cells, and overall cytotoxicity. Cell Painting is a broadly used image-based assay that uses morphological features to capture how cells respond to treatments. However, this method requires cell fixation for staining, which prevents examining live cells. To address this limitation, here we present Live-Cell Painting (LCP), a high-content method based on acridine orange, a metachromatic dye that labels different organelles and cellular structures. We began by showing that LCP can be applied to follow acidic vesicle redistribution of cells exposed to acidic vesicles inhibitors. Next, we show that LCP can identify subtle changes in cells exposed to silver nanoparticles that are not detected by techniques such as MTT assay. In drug treatments, LCP was helpful in assessing the dose-response relationship and creating profiles that allow clustering of drugs that cause liver injury. Here, we present an affordable and easy-to-use image-based assay capable of assessing overall cell health and showing promise for use in various applications such as assessing drugs and nanoparticles. We envisage the use of LCP as an initial screening of overall cell health while providing insights into new biological questions.

SIGNIFICANCE STATEMENT

- Despite the existence of some methods for live-cell profiling, there is a pressing need for assays that are both user-friendly and cost-effective.
- LCP introduces a simple and innovative assay for live-cell investigation, providing image-based profiling, and detailed insights into intracellular events.
- The LCP assay holds significant potential to advance the field of image-based live-cell profiling and could be instrumental in toxicology and drug development research.

Monitoring Editor

Assaf Zaritsky
Ben-Gurion University, Negev

Received: Aug 8, 2024
Revised: Apr 23, 2025
Accepted: Apr 29, 2025

 Instructional Resource

 New Methods

This article was published online ahead of print in MBoC in Press (<http://www.molbiolcell.org/cgi/doi/10.1091/mbc.E24-07-0308>) on May 6, 2025.

Author contributions: F.G.-F., T.M.-L., and M.R.d.S. performed the experiments; F.G.-F., T.M.-L., M.R.d.S., B.D.-R., and M.B.d.J. analyzed the data; F.G.-F., T.M.-L., M.R.d.S., A.E.C., B.A.C., S.S. and M.B.d.J. drafted the article; F.G.-F. prepared the digital images.

Conflicts of interest: The authors declare no financial conflict of interest.

*Address correspondence to: Marcelo Bispo de Jesus (dejesus@unicamp.br).

Abbreviations used: AgNP, silver nanoparticles; AO, acridine orange; CRISPR, clustered regularly interspaced short palindromic repeats; DILI, drug-induced liver injury; GFP, green fluorescence protein; HDBSCAN, hierarchical density-based spatial clustering of applications with noise; iPSCs, induced

INTRODUCTION

Image-based methods for high-content analysis play a pivotal role in uncovering novel mechanisms of action (MOA) and providing insights into drug-induced phenotypes, offering an overview of cell function (Way *et al.*, 2023). Widely applicable across various biological areas, this approach accelerates drug discovery by offering lots of quantitative and qualitative data, facilitating the identification and optimization of lead compounds (Zanella *et al.*, 2010; Lin *et al.*, 2020), and providing chemical toxicological profiles (Li and Xia, 2019). Image-based profiling assays showcase their versatility by not only predicting cell health outcomes (Way *et al.*, 2022) but also revealing intriguing impacts of genetic perturbations, such as those found by CRISPR-Cas9 editing (Lazar *et al.*, 2024). Additionally, this approach can also identify distinctive epigenetic changes induced by compounds, aiding accurate drug-type prediction and even pinpointing drugs associated with reduced tumor regrowth (Farhy *et al.*, 2019). These examples underscore the potential of image-based methods combined with high-content analysis to significantly improve our understanding of biology and to advance applications in various fields, particularly in drug discovery and toxicology.

Furthermore, image-based methods offer a noninvasive means of studying cellular dynamics, allowing for real-time observations and analysis of dynamic processes within cells. Temporal evaluation improves the ability to capture transient events, enabling a more comprehensive understanding of cellular responses (Garvey *et al.*, 2016; André *et al.*, 2023). Applying machine learning algorithms to image analysis enhances the accuracy of extracting meaningful information from complex datasets, further advancing the potential of image-based methods (Siegismund *et al.*, 2022). Finally, the combination of image-based profiling with multiomics data, such as genomics and transcriptomics, provides a holistic understanding of cellular responses, linking morphological changes to underlying genetic, and molecular alterations (Watson *et al.*, 2022). These examples showcase the versatility of image-based methods, which can provide an invaluable tool for studying dynamic cellular processes.

Image-based assays on fixed cells are straightforward and convenient for staining and imaging many samples, but this approach has some limitations. The physical processes of cell fixation and permeabilization can lead to image artifacts, significantly altering intracellular structures, including protein and lipid distribution, and causing the loss of chemical gradients (Schnell *et al.*, 2012). Although fixed-cell imaging involves the preservation of cellular structures at a specific moment in time, live-cell image-based methods allow for detailed temporal examination of cellular components, such as organelle activity (e.g., vesicles acidification, nucleoli organization) and cytoskeletal (Wang *et al.*, 2020). In addition to real-time observation, live-cell imaging facilitates the monitoring of cellular responses to external stimuli over extended periods, providing insights into the kinetics and dynamics of cellular processes (Gordonov *et al.*, 2016). This is particularly valuable in un-

derstanding long-term effects and cellular responses, such as those occurring in chronic diseases or during prolonged drug exposure (Tolosa *et al.*, 2019).

Advances have been made in the field of live-cell imaging through the development of new technologies, but some limitations persist. Establishing cell lines that express fluorescent reporter proteins often requires the constant use of antibiotics, which can result in artifacts by perturbing cell metabolism (Binó *et al.*, 2022; Cuny *et al.*, 2022). Alternatively, using gene-editing technologies offers more precise methods for introducing fluorescent reporters without the need for antibiotics, thereby addressing some challenges associated with live-cell imaging. However, the widespread use of this technology still faced some limitations, such as large array sizes, the lack of an efficient gene delivery system, and high associated costs (Huang *et al.*, 2023). Although some approaches enable live-cell profiling, there remains an urgent need for new assays that are both user-friendly and cost-effective.

Here, we present live-cell painting (LCP), which uses acridine orange (AO) to stain live cells for image-based profiling. AO metachromatic fluorescence can report on different cellular chemical microenvironments and has been widely used to track and evaluate acidic vesicles in various cell models. This has been explored in conjunction with other markers, such as LysoTracker Red and quinacrine, which are also used as fluorescent probes for tracking acidic vesicles (Pierzyńska-Mach *et al.*, 2014). Additionally, an elegant approach demonstrated that ratiometric analysis of AO staining can serve as an initial and quantitative method for evaluating the late stages of autophagy in individual cells (Thomé *et al.*, 2016). AO monomers intercalate between neighboring pairs of DNA and RNA, absorbing blue light (~458 nm) and emitting green light (~530 nm). At higher concentrations in cells, AO interacts electrostatically with DNA and RNA and can also organize into stacks and accumulate in acidic vesicles. When AO is organized as stacks, it will shift the emission spectra to red light (~640 nm). To establish LCP, we optimized AO concentration, evaluated its versatility across different cell lines, and determined nontoxic concentrations. We next validated AO affinity for acidic vesicles and the ability to track vesicle redistribution and cell phenotype assessment. To demonstrate image-based profiling capacity and versatility, we used different perturbations: silver nanoparticles and drugs. Using silver nanoparticles, we demonstrated the ability of LCP to assess the dose-response relationship. For drug assessment, cells were treated with selected compounds from the drug-induced liver injury (DILI) rank list, and data were grouped into profiles based on images depending on concentration and compound. Our results demonstrate that LCP holds promise as an easy-to-use method for image-based profiling and analysis of individual features in living cells, providing valuable insights into cell health and condition.

RESULTS

LCP: broadly applicable to cell lines and cytotoxicity assessment

To establish the LCP for image-based profiling, we began by assessing the cytotoxic profile of cells exposed to AO using the CellTiter-Glo Luminescent Cell Viability Assay. Our goal was to identify an optimal AO concentration that ensures cell viability while allowing effective staining of nucleic acids and acidic vesicles. For this purpose, we selected four cell lines: Huh-7 (hepatocarcinoma), MCF-7 (breast cancer), PNT1A (non-cancer prostate epithelium), and PC-3 (prostate cancer) (Supplemental Figure S1). Cells were treated with increasing concentrations of AO (2.5, 5.0,

pluripotent stem cell; LCP, live-cell painting; MOA, mechanisms of action; MTT, 3-(4,5-dimethylthiazol-2-yl)-2,5-diphenyltetrazolium bromide; NMDA, N-methyl-D-aspartate; PI, propidium iodide; t-SNE, t-distributed stochastic neighbor embedding; UMAP, uniform manifold approximation and projection.

© 2025 Garcia-Fossa *et al.* This article is distributed by The American Society for Cell Biology under license from the author(s). It is available to the public under an Attribution 4.0 International Creative Commons CC-BY 4.0 License (<https://creativecommons.org/licenses/by/4.0/>).

"ASCB®," "The American Society for Cell Biology®," and "Molecular Biology of the Cell®" are registered trademarks of The American Society for Cell Biology.

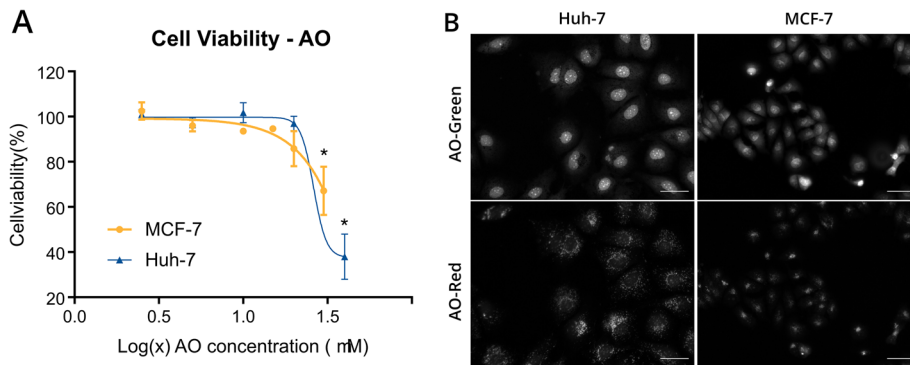


FIGURE 1: Cell viability in the presence of AO assessed by ATP concentration. Huh-7 and MCF-7 cells were plated at a density of 8000 cells per well in a 96-well plate. After 24 h, cells were treated with AO (2.5, 5.0, 10.0, 20.0, and 40.0 μM) for 4 h. Then, viability was assessed using CellTiter-Glo by measuring ATP concentration with luminescence. ATP concentration in the cells was determined by fitting a linear function to the ATP standard curve and calculating the relative viability compared with the negative control. (A) Viability curve for Huh-7 and MCF-7 cells exposed to AO. (B) Representative images were acquired (Cytation 5, 20 \times objective) for Huh-7 and MCF-7 cells exposed to 20 and 10 μM of AO, respectively, represented by the AO-green and AO-red channels. Scale bar, 50 μm . Statistical test performed with two-way ANOVA followed by Sidak's multiple comparisons test: * $p < 0.05$.

10.0, 20.0, and 40.0 μM) for 4 h, estimating the time cells would be exposed to AO during image acquisition.

Cells exhibited distinct tolerances when exposed to AO. Huh-7 cells tolerated up to 20 μM of AO for 4 h, showing no significant difference ($p > 0.05$) compared with the negative control (Figure 1A, data normalized to untreated cells). At higher concentrations (40 μM , corresponding to 1.6 on the logarithmic scale, Figure 1A), cell viability was significantly reduced ($p < 0.05$) to $\sim 40\%$. Therefore, we chose 20 μM to proceed with the following experiments. MCF-7 cells tolerated higher concentrations of AO, as cell viability was only significantly reduced ($p < 0.05$) to $\sim 70\%$ at 40 μM AO, revealing a cell-typedependent response (Figure 1B). Prostate cells (PNT1A and PC-3) showed even lower tolerance to AO exposure; the maximum AO concentration that did not affect cell viability was 2.5 μM (Supplemental Figure S1). Higher AO concentrations did not significantly reduce cell viability in prostate cells; however, they caused pronounced morphological changes (e.g., diminished distinction between the nucleus and cytoplasm), which influenced our decision to use the 2.5 μM concentration. In Figure 1B, in the AO-Green and AO-Red channels, we visualized cellular components like the nucleus and acidic vesicles, respectively. These images highlight that while cell viability was a key factor in selecting the optimal AO concentration, preserving cellular morphology was equally critical to ensure accurate structural visualization. This dual-channel approach provides insights into the cellular structures and functions under investigation. We conclude that cell tolerance to AO is cell type dependent; therefore, it is imperative to evaluate cell viability to determine the AO concentration with minimal toxicity while maintaining its ability to stain cell compartments.

AO captures the dynamics of acidic vesicles

To validate AO accumulation in acidic vesicles (late endosomes and lysosomes) and to illustrate that AO can be used to detect vesicle (re)distribution, we used two well-known acidification inhibitors: bafilomycin A1 and chloroquine. Our underlying hypothesis was that treatment with these inhibitors would result in a reduction in fluorescence intensity and potentially alter the distribution of vesicles in the cytoplasm. To assess this hypothesis, we incubated Huh-7 cells with inhibitors (bafilomycin A1 1 μM , and chloroquine, 50 μM) for 0.5 or 4 h and used either LysoTracker

Deep Red or AO to follow acidic vesicle distribution. LysoTracker was used to confirm the presence of acidic vesicles in control cells and validate the decrease in fluorescence intensity upon inhibitor treatment (Supplemental Figure S2).

Vesicle morphology changed upon incubation with the inhibitors, showing changes in the distribution, number, and intensity of acidic vesicles over time (Figure 2B). After segmentation of cell borders, the total intensity of AO across all cells was calculated by multiplying the cell number by the mean AO-Red cell intensity (Figure 2A). Bafilomycin A significantly decreased overall intensity at 0.5 and 4 h ($p < 0.05$). Intriguingly, chloroquine significantly increased the total intensity after 0.5 h of treatment and subsequently decreased to levels similar to those of untreated cells after 4 h of treatment. AO begins to accumulate in the cell nuclei after 4 h of treatment with bafilomycin A and chloroquine (Figure 2B). This profile differs from the untreated cells, indicating a subtle toxic effect after 4 h. However, control staining with Rab7, a marker of late endosomes, revealed no overt changes in the distribution of Rab7-positive vesicles following treatment (Supplemental Figure S3). This suggests that the observed AO signal dynamics may not solely reflect changes in vesicle abundance or localization, but could also be influenced by altered dye uptake or accumulation. These results emphasize the need for caution when interpreting AO-based phenotypes, as they may reflect perturbations in dye accumulation rather than only structural changes in acidic compartments.

The LCP assay can also report the patterns of acidic vesicle distribution across the cell. To assess acidic vesicle distribution across the cell, we used a CellProfiler module called MeasureObjectIntensityDistribution, which divides cells into four concentric rings and measures the fraction of the cell's staining intensity in each ring in the AO-Red channel (Figure 2B). For bafilomycin A1, the intensity at ring three decreased at 0.5 and 4 h, revealing a pattern of change in the morphology of the treated cells. Chloroquine shows a similar pattern of vesicle distribution compared with untreated cells, while bafilomycin A1 shows a distinct distribution that persists throughout 4 h of treatment (Figure 2C). Collectively, these findings suggest that AO successfully captured the cellular state of acidic vesicles, and this approach can provide fine details about the cell response to perturbation.

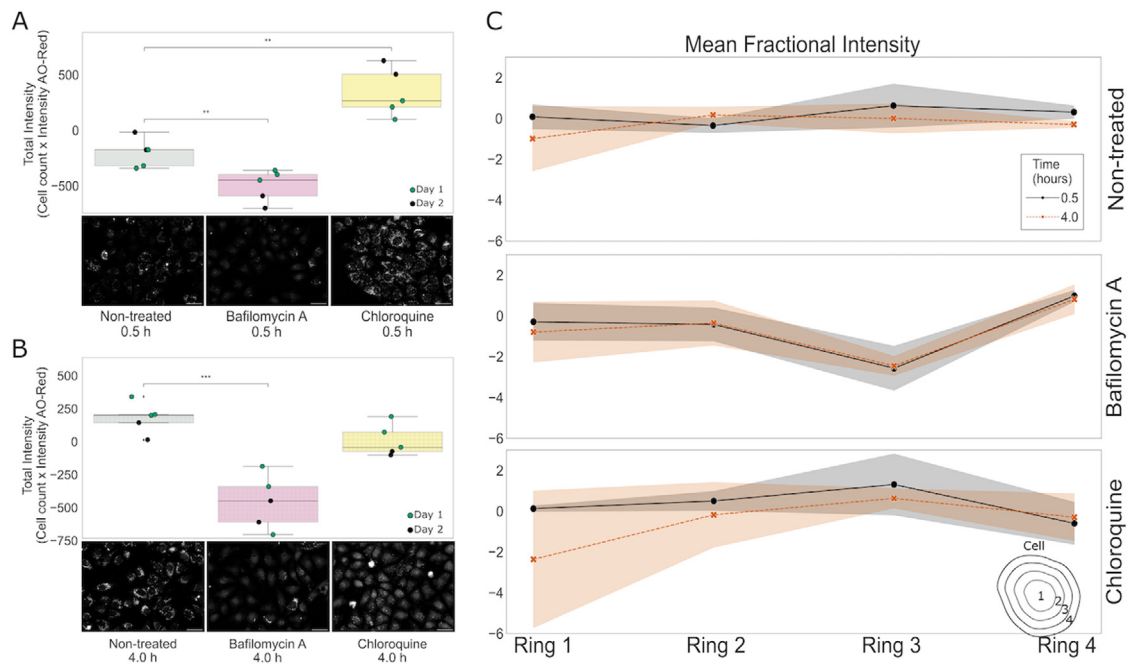


FIGURE 2: AO assessment of acidic vesicle dynamics in Huh-7 cells. Huh-7 cells were plated at 8000 cells per well into 96-well plates. The next day, cells were treated with bafilomycin A 1.5 μ M + AO or chloroquine 50 μ M + AO for 0.5 or 4 h. Subsequently, the medium was replaced with fluorobrite, and images were captured using the Cytation 5 BioTek system, with a 20 \times objective. The AO-red intensity values for bafilomycin A and chloroquine are normalized to the nontreated cells. (A and B) The total AO-red intensity, which stains acidic vesicles, was quantified as the mean integrated intensity in the cytoplasm. Each point represents aggregated well-level data, color-coded by batch. Below each graph, representative images show Huh-7 cells with and without inhibitors at the respective exposure times (0.5 or 4 h). Scale bar, 50 μ m. (C) Each identified cell was split into four concentric rings using CellProfiler, and the intensity was measured in each concentric ring. The mean fractional intensity is represented in each concentric ring (1 of 4, 2 of 4, 3 of 4, and 4 of 4). The intensity at each concentric ring is shown in the x-axis, starting from the center of the cell (1 of 4) to the border of the cell (4 of 4). Experiments were performed in two independent replicates, $n = 3$ wells. A statistical test (independent t-test) was performed using the statannotations library. * p statistical difference < 0.05.

AO captures dose-response effects

To illustrate how AO can be used to identify perturbations to cells caused by dose-response treatments, we treated cells with increasing concentrations of silver nanoparticles for 24 h. Nanoparticles exploit unique properties at the nanometer scale and provide solutions to various problems, particularly in areas such as nanomedicine. However, their use also poses challenges due to possible undesirable effects, in particular toxic effects when reaching eukaryotic cells. Here, we used nanoparticles in two sizes: 40 (referred to as Ag40; Supplemental Figure S6) and 100 nm (referred to as Ag100). To determine whether AO intensity is affected by nanoparticle concentration, we measured AO-Green and AO-Red intensity per cell under each treatment condition. Our results indicate that total AO intensity per well (Green and Red) increased with higher AgNP concentrations, even as the number of acidic vesicles decreased (Supplemental Figure S5). This suggests that AO uptake per cell was not impaired by the treatments and may have been enhanced. The t-SNE (t-distributed stochastic neighbor embedding) algorithm was used for dimensionality reduction and visualization (Figure 3A), providing insight and intuition into different AgNP treatment patterns. Higher concentrations of Ag100 are located at the top left, while lower concentrations are located at the bottom right, suggesting that AO has the potential to identify dose-response changes. We also compared the sensitivity of LCP with the MTT assay, a traditional method for assessing cell viabil-

ity. Concentrations detectable by LCP were up to 40 times lower than the IC₁₀ value, based on values previously determined with MTT (i.e., the inhibitory concentration of 10% of the population), indicating a greater sensitivity.

To confirm the dose-response profiles observed in the t-SNE representation, we used two approaches to identify the most important features that distinguish between the negative control and the highest concentrations of Ag100. First, we used Morpheus software's (<https://software.broadinstitute.org/morpheus/>) marker selection tool to perform a t-test and provide the 30 most important features. Additionally, we used random forest to rank features by their importance using bootstrapping. Among the 30 most important features, eight features matched between the models. For these features, we plot their fold change relative to the negative control (Figure 3B), ranging up to 6 times higher or lower than the negative control. To further investigate the dose-response effect on specific features, we chose the two features that had the highest negative or positive response related to the negative control (the first and last feature in the y-axis in Figure 3B), Cytoplasm_Texture_Entropy_CorrPI_20_03_256 and Nuclei_AreaShape_SpatialMoment_1_3 (Figure 3, C and D) and identified a strong dose-response effect to increasing Ag100 concentrations. The six remaining features that also presented strong dose-response behavior are available in Supplemental Figure S7.

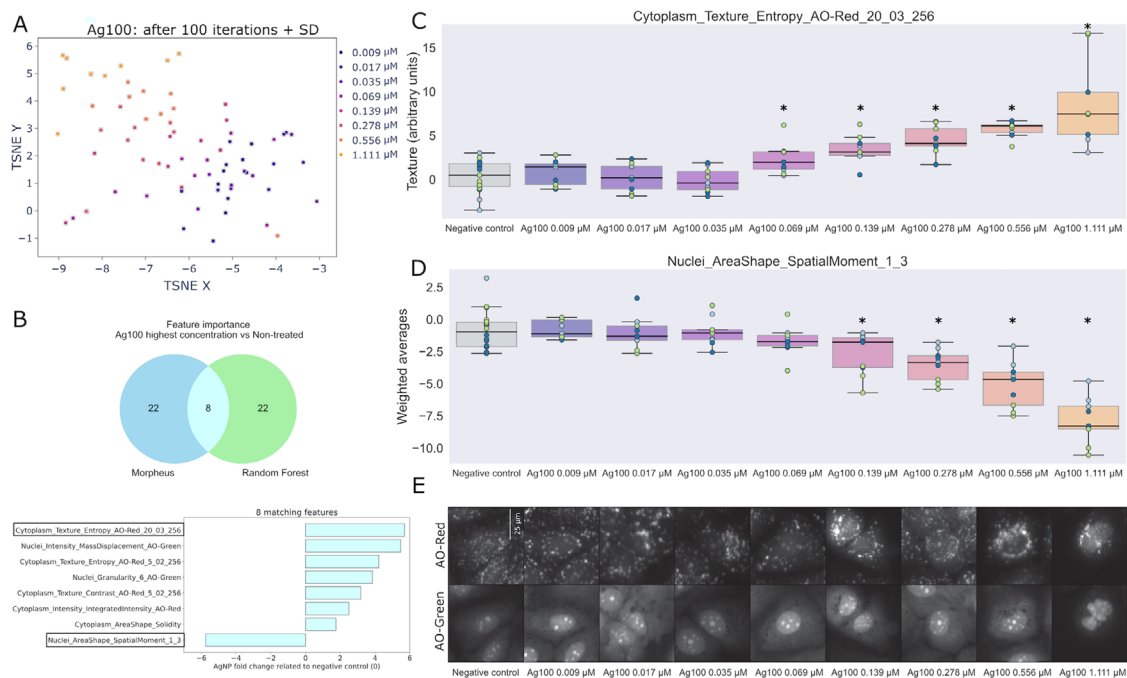


FIGURE 3: AO captures the dose-response effect induced by silver nanoparticles (AgNPs) on Huh-7 cells. Huh-7 cells were treated with Ag100 (nanoparticle size 100 nm) at increasing concentrations for 24 h. Then the images were acquired after AO staining (Cytation 5, 20 \times objective). Objects were segmented using Cellpose software, and features were extracted using CellProfiler software. Next, features were aggregated by well, normalized, and selected using Pycotminer and batch corrected using pyComBat. (A) t-SNE was used for dimensionality reduction and visualization. After 100 iterations, the mean and SD embedding were calculated. Because the profiles were normalized relative to the negative control, these were not included in the plot. (B) Random forest ran for 100 iterations to differentiate between two classes: negative control versus combining Ag100 0.556 and 1.111 μM . Then, the mean feature importance and SD were calculated. Morphheus software was used to perform marker selection between the same random forest classified groups, and the top 30 features were selected and compared. Among those, eight features were consistent between methods and were plotted to show the fold change compared with the negative control. The two features highlighted by black boxes are presented in C and D; (C) Texture entropy in the cytoplasm measured in the AO-red channel. Entropy represents the complexity of the image, with higher values, indicating greater heterogeneity in fluorescence intensity patterns; (D) The spatial moment of the nuclei, representing the shape, size, rotation, and location of the nuclear object; and (E) Representative images were retrieved from the dataset using *k* means clustering (Garcia-Fossa et al., 2023). Experiments were performed in three independent replicates, $n = 3$ and each point in the plots consists of well-aggregated data, and the points are colored by the batch in C and D. An independent *t* test calculated using the statannot library. **p* statistical difference < 0.05. Scale bar, 25 μm .

The representative images (Figure 3E), retrieved using *k* means clustering (Garcia-Fossa et al., 2023), illustrate substantial effects on cell size and intensity in both channels, in cells treated with Ag100. From concentrations of 0.139 μM onward, the size of the cells begins to shrink, which is reflected in the irregular shape of the nuclei. This can be quantified using the SpatialMoment function, which is a series of weighted averages that provide information about the object's shape, dimensions, orientation, and position (Figure 3D). Interestingly, both features reveal statistically significant changes in the cells at lower dose points than the IC₅₀ value previously determined by the MTT assay (Ag100 IC₅₀ value determined by MTT was 0.042 μM vs. 2.937 μM determined by fitting a curve to Figure 3C). These results demonstrate that the LCP successfully provided dose-response analysis and, based on morphological changes, exhibited greater sensitivity than the MTT assay.

LCP for profiling hepatocytes undergoing DILI

After showing that LCP captures details about intracellular organization and that this could be sensitive enough to reveal how cells respond to perturbations, we hypothesized that LCP could be used

in image-based profiling. To test this hypothesis, we treated Huh-7 cells with six compounds present in the DILI-rank dataset (Chen et al., 2016). We then tested whether the cells could be grouped by the compound based on the induced phenotype in hepatocytes. The drugs (1036) are divided into four classes based on their potential to cause liver injury: no DILI concern, less DILI concern, major DILI concern, and equivocal DILI concern. We used lactose and untreated cells as negative controls. Among DILI compounds, six were selected and used to treat cells for 24 h (Table 1); cells were then stained with AO and prepared for imaging. To ensure that AO staining did not interfere with cell viability within our experimental conditions, we assessed the cytotoxicity of all tested compounds in the presence and absence of AO (Supplemental Figure S13). No significant differences were observed between the two conditions, confirming that AO does not introduce measurable toxicity within this timeframe. To assess whether AO localization was altered by the treatments, we measured the integrated AO-Green intensity, reflecting DNA/RNA staining, within nuclei and across whole cells (Supplemental Figure S5, A and B). The ratio of nuclear to whole-cell AO intensity (Supplemental Figure S5C) remained

Compound	Concentration (μM)	MOA	DILI-concern/severity class
Untreated cells	0	Negative control	—
Lactose	1 and 10	Negative control	—
Aspirin	1 and 10	COX inhibitor (Henry et al., 2017; Yang et al., 2017)	Less-concern/class 0
Orphenadrine citrate	1 and 10	Histamine/NMDA receptors inhibitor (Kornhuber et al., 1995; Rumore and Schlichting, 1985)	Less-concern/class 0
Etoposide	1 and 10	Topoisomerase II inhibition (Montecucco et al., 2015)	Less-concern/class 3
Lovastatin	1 and 10	HMG-CoA reductase inhibitor (Duong and Bajaj, 2023)	Less-concern/class 3
Cyclophosphamide	1 and 10	DNA alkylation (Ogino and Tadi, 2023)	Less-concern/class 5
Amiodarone	0.2 and 2	Sodium/potassium-ATPase inhibitor (Anthérieu et al., 2010; Florek et al., 2023)	Most-concern/class 8

TABLE 1 : Compounds used to treat cells for the DILI drug-screening assay, concentrations used, and described MOA. The DILI-concern and -severity class were based on the DILI-rank dataset (Chen et al., 2016).

unchanged across all treatments, indicating that none of the tested compounds caused a notable shift in AO distribution between nuclear and cytoplasmic compartments. However, interference could, in theory, exist for any given compound and should be tested to see whether it impacts mechanistic conclusions.

All cells treated with the compounds were phenotypically active, meaning that their replicate image-based profiles are statistically retrievable relative to negative controls (mean Average Precision [mAP] > 0.05, except for orphenadrine 1 μM that was filtered out) (Kalinin et al., 2024). Some compounds formed more distinct clusters than others. For example, orphenadrine and etoposide showed clear clustering as detected by LCP profiling (Figure 4A), which was further confirmed by unsupervised machine learning algorithm clusters based on density (Figure 4B). The clustering was not determined by the DILI severity class, where only the 0-class is identified as a cluster (Figure 4C). Representative images of single cells treated with DILI drugs and negative control were retrieved from the dataset using *k* means clustering (Garcia-Fossa et al., 2023) (Figure 4D).

To examine the features captured by LCP able to distinguish treated cells from the negative control, we used the same approach as in the section above. We identified the 100 most important features using random forest ensembles and Morpheus *t* test for each compound against the negative control, resulting in 50 features matching between the random forest and Morpheus approaches. We found that texture-related features were important to determine the profile of the DILI compounds, followed by intensity, area-shape, and granularity (Figure 4E). Therefore, we show that LCP captures the phenotypic profile of DILI-ranked drugs and provides phenotypic pathway visualizations for each compound.

To understand the patterns of morphological effects in which features were altered by the treatments, we group the features into six categories (area-shape, intensity, texture, correlation, granularity, and radial-distribution), as well as features separated by channel (AO-Green, AO-Red, and area-shape) (Supplemental Figure S12). Of the top 50 features, 52% belong to the AO-Red channel when cells are treated with amiodarone, and 90% in cells treated with lovastatin (Supplemental Figure S12). Despite amiodarone and lovastatin having different MOAs (Table 1), their phenotypic profiles are similar. They are classified into the same class by HDBSCAN (hierarchical density-based spatial clustering of applications with noise), an unsupervised clustering algorithm based on density (Figure 4B, class 3). These two compounds share 30% of their most important features (Supplemental Figure S12), all of which belong to the AO-Red channel and are largely related to the texture and radial distribution of intensity in the AO-Red channel, which may be linked to changes in the distribution of acidic vesicles. Another similarity is

that amiodarone and lovastatin induce direct or indirect disruption of the mitochondrial respiratory chain (Donato and Tolosa, 2021), leading cells to present a similar phenotype.

For compounds that presented a stronger profile—etoposide and orphenadrine—we split the important features into higher or lower values relative to the negative control, categorizing them as increased or decreased compared with the baseline. The features were then analyzed regarding compartment, channel, feature subgroup, and their fold change related to the negative control (Figure 4F). Both compounds induce different phenotypes that are distinguishable in the representative images (Figure 4D) and also in the clustering, each assigned to a class (Figure 4B, class 1 for orphenadrine and class 2 for etoposide). Etoposide, a topoisomerase II inhibitor, induces significant nuclear structural changes characterized by increased texture correlation and granularity in nuclei (Figure 4F; Supplemental Figure S14). Additionally, treated cells exhibit a 5-fold increase in Cytoplasm_AreaShape_Perimeter, indicating cellular enlargement (Supplemental Figure S14D). Orphenadrine binds and inhibits both histamine H1 and NMDA receptors, and it is classified as safe for the liver (class 0 in DILI severity). Analysis of its effects on Huh-7 cells revealed elevated values in vesicle area, shape and eccentricity, suggesting potential alterations in vesicular trafficking or cellular secretory pathways. Conversely, reduced intensity measures in nucleoli and cytoplasmic mass displacement may indicate lowered metabolic activity or changes in protein synthesis (Figure 4F; Supplemental Figure S15). These adaptations likely represent responses to cellular stress or shifts in metabolic demands within liver cells. By linking these features to specific aspects of etoposide's and orphenadrine's action, we can better understand the cellular responses and validate the use of AO for assessing the drug's effects. These results demonstrate that LCP can be a useful tool for determining the phenotypic profile in living cells and provide mechanistic insights into visualizing phenotypic pathways for each activity group.

DISCUSSION

Here, we propose the LCP assay, an informative image-based assay that can be performed in living cells using AO as a fluorescent dye. Leveraging the dual-emission property of AO allows for distinguishing many intracellular structures, including nucleic acids and acidic compartments such as late endosomes and lysosomes. We show that LCP provides a wealth of information by monitoring the morphological changes of cell populations in response to perturbations such as drugs or nanoparticles. With these perturbations, we have gained additional insights into the LCP, highlighting its capacity to cover a wide range of phenotypes, such as clustering

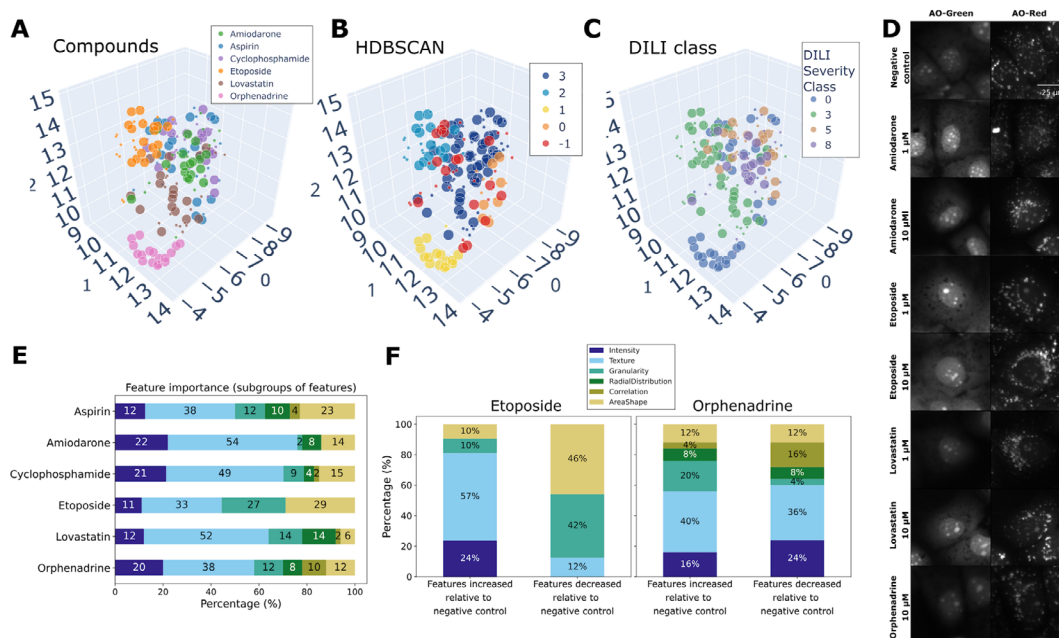


FIGURE 4: LCP captures the phenotypic profile of Huh-7 cells treated with drugs from the DILI-rank. Huh-7 cells were treated with drugs at the indicated concentrations (Table 1) for 24 h. After that, cells were stained with AO, and images were acquired using the Cytation 5 20 \times objective in the AO-green and AO-red channels. The images were processed with cell segmentation and feature extraction using Cellpose and CellProfiler. Next, the data were aggregated by well, normalized, and feature-selected using pycytominer and batch-corrected using pyCombat. (A) UMAP (cosine metric) was used to reduce the dimensionality of \sim 300 features. The data were color-coded for each drug and the size of the dots represents the dose of the compounds (lower concentrations are smaller and higher concentrations are larger). Because the profiles were not normalized relative to the negative control, these were not included in the plot; (B) Samples were classified using unsupervised HDBSCAN clustering. Noisy samples are given the label-1; (C) UMAP labeled by DILI-severity class; (D) Representative images of single cells; and (E) Matching features between random forest and Morpheus (50) were categorized into subgroups. (F) Features increased or decreased relative to the negative control were categorized into subgroups for etoposide and orphenadrine. The experiments were performed in five independent batches with four replicates each.

DILI drugs. Additionally, it was highly sensitive to detect perturbations, such as those at low concentrations of nanoparticles, which are crucial for several processes reflected in cell morphology.

We found that LCP can be used to study specific cellular mechanisms, such as acidic vesicle dynamics. AO staining captures details of acidic vesicles distribution, demonstrated by using acidification inhibitors and by analyzing the AO-Red intensity within concentric rings in the cell. Bafilomycin A1, which inhibits autophagosome-lysosome fusion and acidification (Yoshimori *et al.*, 1991), significantly reduced the number and intensity of acidic vesicles in Huh-7 cells, consistent with its role in preventing autolysosome formation. Conversely, chloroquine, known for its inhibition of autophagy and lysosomal function (Homewood *et al.*, 1972), induced phospholipidosis in hepatocytes. This condition was characterized by the accumulation of phospholipids in lysosomes, resulting in stronger AO staining of acidic vesicles compared with untreated cells (Cho *et al.*, 2020). These findings demonstrate the assay's capability to capture specific morphological details of intracellular events induced by pharmacological interventions.

Furthermore, LCP revealed dose-response effects in cell responses to silver nanoparticles (AgNP) and other perturbations. This approach uses a single dye as opposed to other assays, such as the original cell painting assay (Bray *et al.*, 2016; Cimini *et al.*, 2023) that requires six dyes added in two staining steps. Our method has demonstrated its ability to uncover subtle changes in treated cells that are often missed by conventional techniques such as MTT

assays (Supplemental Figure S9). In our dose-response assay with low concentrations of AgNP, we observed alterations in acidic vesicle distribution and cell size, potentially linked to autophagy pathways. Previous studies on various cell types and nanoparticles suggest that cells might utilize the endolysosomal pathway to process AgNP (Ha *et al.*, 2014; Nakashima *et al.*, 2019). Dysregulation of autophagy, induced by pathway inhibition or excessive stimulation under external stressors, could explain these observations.

Moreover, LCP provided insights into the MOA of drugs based on cell phenotypes. Amiodarone induced phospholipidosis in HepaRG cells by short-term exposure to the drug (Anthérieu *et al.*, 2010), and alterations shown by AO staining in vesicle morphology and spatial distribution patterns (normalized moments and eccentricity) suggest that amiodarone might impact vesicular trafficking and dynamics (Supplemental Figure S13). Similarly, AO staining reveals significant insights into etoposide's MOA by showing increased texture correlation and granularity in nuclei, indicative of the drug's effect on nuclear morphology and its role in inducing DNA damage responses. These changes are consistent with etoposide's mechanism as a topoisomerase II inhibitor, leading to cell-cycle arrest and apoptosis (Montecucco *et al.*, 2015). Conversely, despite its classification as safe for the liver (class 0 in DILI severity), Orphenadrine's impact on cellular structures and dynamics in Huh-7 cells reveals subtle effects through AO staining. This includes alterations in vesicle morphology and reduced measures of nucleoli and cytoplasmic mass displacement, suggesting potential changes

in cellular protein synthesis and metabolic activity (Rumore and Schlichting, 1985; Kornhuber et al., 1995). Overall, LCP enabled comprehensive assessments of cell health and morphological profiles under various treatment conditions, promising scalability for large-scale and cost-effective applications in the future.

Our results establish a live-cell proof-of-concept framework for detecting intracellular events and profiling morphological changes using AO and high-content microscopy. Although our framework successfully demonstrates its utility in assessing acidic vesicle dynamics and cellular morphological profiles, some limitations require consideration. For instance, we observed photobleaching in the AO-Green and AO-Red channels during repeated imaging sessions (10 consecutive acquisitions spaced 10 s apart), which suggests the need for improvements in AO's photostability for extended kinetic studies (data not shown). Furthermore, caution is advised in interpreting AO staining, necessitating comparison with ground truth annotated compounds to validate new drug profiling. AO primarily assesses nucleic acids and acidic vesicles, thereby indirectly indicating alterations in numerous cellular signaling pathways. Moreover, optimizing AO concentrations to balance staining intensity and cytotoxicity remains a challenge across different cell lines, often requiring the integration of alternative stains like Hoechst to enhance contrast without compromising cell viability. This challenge becomes even more pronounced in coculture applications, where a single AO concentration must be carefully optimized to suit multiple cell types without introducing toxicity or compromising imaging quality. It should always be considered that any perturbation can alter AO staining patterns. Drug treatments may interfere with AO interactions with nucleotides or acidic vesicles, and any unexpected AO behavior should be validated with additional sanity check experiments. Additionally, future work could extend AO-based profiling to more complex cell types, including iPSCs, progenitors, and iPSC-derived cells, which may present unique staining and viability challenges. Despite these challenges, our approach holds promise for broad applications across diverse cell types, diseases, and biological inquiries. Future studies should focus on evaluating AO's efficacy in discerning varied phenotypes and MOA across a wider range of compounds, potentially integrating clinical samples and multiomics data to enhance its clinical relevance and applicability.

CONCLUSION

Live-cell painting represents a straightforward assay for investigating live cells, offering an image-based profile and detailed insights into intracellular events. The LCP captures acidic vesicle dynamics and cellular response to low concentrations of nanoparticles and generates hypotheses about the interaction between nanoparticles and cells. In addition, it is used to define groups of cells based on their phenotype after treatment with drugs that induce liver injury. AO is a suitable dye for image-based profiling, providing interesting information about the condition and health of cells while providing insights for new biological questions/research. We believe the assay could benefit the field of image-based live-cell profiling and potentially be used in toxicology and drug development in the future.

MATERIALS AND METHODS

[Request a protocol through Bio-protocol](#)

Cell culture

Huh-7 human hepatoma cells (no. JCRB0403), hereinafter referred to as Huh-7, were obtained from the Japanese Collection of Re-

search Bioresources Cell Bank (JCRB, Japan). Cells were maintained in culture in DMEM (Life Technologies, Canada) supplemented with 10% FBS (Life Technologies, South America) and 1% antibiotics (penicillin/streptomycin, Pen/Strep) (Life Technologies, GI). Cells were incubated in a Panasonic incubator at 37°C, 95% humidity, and 5% CO₂ and were passed as required for maintenance when confluency reached ~80%. Cultures were determined to be free of *Mycoplasma* at each thaw using the direct DNA staining method (with Hoechst 33342 [Invitrogen]) and inspected under fluorescence microscopy. All experiments were performed with cells free of *Mycoplasma*.

AO staining

Huh-7 cells were plated at a density of 8000 cells per well in 96-well plates and grown in DMEM medium supplemented with 10% FBS and 1% Pen/Strep. After 24 h, the cells were treated in triplicate with 100 µl of a range of AO concentrations (2.5, 5, 10, 20, and 40 µM) diluted in a nonsupplemented medium (serum-free). Then, cells were incubated for 10 min at 37°C and 5% CO₂. After 10 min, the AO solutions were replaced by 100 µl of FluoroBrite DMEM (Life Technologies). Fluorescence images were acquired on Cytation 5 Hybrid Multidetector Reader (BioTek Instruments, Winooski, VT), from herein called Cytation 5, using the filter cubes from BioTek named green fluorescence protein (GFP; excitation/emission = 469/525 nm) and propidium iodide (PI; excitation/emission = 531/647 nm). A 20× with NA 0.45 objective was used, with a pixel size of 0.321895 µm/pixel (equivalent to 3.106599 pixels/µm). Each well was imaged across 16 fields of view, with an image resolution of 1224 × 904 pixels and a bit depth of 16 bits.

ATP viability test

We chose to assess cell viability by quantifying ATP (adenosine triphosphate) using the luminescence signal because AO interferes with common viability assays such as MTT, neutral red, and calcein AM. The ATP viability assay was performed according to the manufacturer's instructions. Briefly, CellTiter-Glo Buffer and lyophilized CellTiter-Glo Substrate (Promega) were placed in the bead bath to reach room temperature. Subsequently, the entire content of CellTiter-Glo Buffer was mixed with the lyophilized CellTiter-Glo Substrate. The mixture was vortexed to obtain a homogeneous solution, forming the CellTiter-Glo Reagent. Huh-7 cells were plated at a density of 8000 cells per well in 96-well plates and grown in DMEM medium supplemented with 10% FBS and 1% Pen/Strep. The cells were treated in triplicate with 100 µl of a range of AO concentrations (2.5, 5, 10, 20, and 40 µM) diluted in nonsupplemented medium (serum-free) and 100 µl of nonsupplemented medium only (negative control), and incubated for 4 h at 37°C and 5% CO₂. After 4 h of treatment with AO, 100 µl of CellTiter-Glo Reagent was added on top of the treatments. The plate was shaken for 2 min on an orbital shaker to induce cell lysis. Subsequently, the contents of the plate were transferred in the same order to an opaque white 96-well plate (suitable for luminescence reading). Then, the plate was incubated at room temperature for 10 min to stabilize the luminescent signal. Subsequently, the luminescence of the wells was read in Cytation 5. The luminescence value was normalized as a percentage of the luminescence value in wells treated only with culture medium (which was considered 100%).

Acidification inhibitors assay

Huh-7 cells were plated into a 96-well plate in a 8000 cells/well. After 24 h of incubation in a Panasonic incubator at 37°C,

95% humidity, and 5% CO₂, the cells were treated with vesicle acidification inhibitors chloroquine 50 μM (Cayman Chemical Company) and bafilomycin A 1.5 μM (Cayman Chemical Company) mixed with either AO 20 μM or LysoTracker Deep Red (Thermo Fisher Scientific) at 75 nM. Cells were treated for 0.5 and 4 h, then the treatment was removed, and FluoroBrite DMEM (Life Technologies) was added for image acquisition. Sixteen sites were acquired per well using 20× Olympus objective plan fluorite NA 0.45 (1320517) with Cytation 5 Hybrid Multidetection Reader (BioTek Instruments, Winooski, VT). Images from LysoTracker Deep Red were acquired using CY5 led cube (excitation/emission = 628/685 nm), and from AO-treated cells using GFP (excitation/emission = 469/525 nm) and PI (excitation/emission = 531/647 nm) filters. The total intensity was calculated by multiplying the “Cells_Intensity_IntegratedIntensity_AO-Red,” a feature that represents the total pixel intensity in each cell in the AO-Red, by the total number of cells analyzed. The radial distribution presented was calculated by dividing the cells into four concentric rings and measuring the intensity of PI in each concentric ring.

Dose-response assay for silver nanoparticles

Huh-7 cells were plated in a 8000 cells/well in a 96-well plate and incubated in a Panasonic incubator at 37°C, 95% humidity, and 5% CO₂. After 24 h, cells were treated with silver nanoparticles (AgNP) of size 40 nm (Ag40) or 100 nm (Ag100) (Sigma-Aldrich, 730807-25ML and 730777-25ML). The concentrations tested for Ag100 were 0.009, 0.017, 0.035, 0.069, 0.139, 0.278, 0.556, and 1.111 μM, and for Ag40 were 0.0011, 0.0022, 0.0043, 0.0087, 0.0174, 0.0347, 0.0694, and 0.1389 μM. Cells were treated for 24 h with the concentrations stated. Then, AO 20 μM was added for 10 min, and the media were replaced with 100 μl of FluoroBrite DMEM (Life Technologies) for image acquisition. The same test was done in parallel to assess the cell viability using MTT at 5 μg/mL (3-(4,5-dimethylthiazol-2-yl)-2,5-diphenyltetrazolium Bromide) (Invitrogen). Sixteen sites per well were acquired using a 20× Olympus objective plan fluorite NA 0.45 (1320517) in Cytation 5 Hybrid Multidetection Reader (BioTek Instruments, Winooski, VT), with the incubator on to maintain 37°C and 5% CO₂. Images from AO were acquired using GFP (excitation/emission = 469/525 nm) and PI (excitation/emission = 531/647 nm) filters. Sixteen sites per well were acquired, and data were processed and analyzed according to the image processing and profiling described below.

Drug-screening assay

Huh-7 cells were plated at a cell density of 8000 cells per well in a 96-well plate. The cell suspension was carefully added to each well, ensuring uniform distribution. The plated cells were allowed to sediment at the bottom of the wells by leaving the plate undisturbed inside the hood for 20 min. Subsequently, the plate was transferred to the cell culture incubator and left undisturbed until the following day to allow cell adhesion and growth. Twenty-four h later, the compounds were prepared by diluting them to concentrations of 1 and 10 μM using an incomplete DMEM medium. The cells were treated with the respective compound solutions (Table 1) for 24 h. Each replicate was performed on different days, and unique plate layouts were designed for each day to account for potential day-to-day variations. On the next day, the culture medium was aspirated, and subsequently, 100 μl of AO solution at 20 μM concentration, was added to each well for cell staining. After a 10-minute incubation, the AO solution was aspirated, and 100 μl of FluoroBrite DMEM (Life Technologies) medium was added to each well. Then, 25 sites per well were acquired using a 20× Olympus

objective plan fluorite NA 0.45 (1320517) in the fluorescence microscope Cytation 5 Hybrid Multidetection Reader (BioTek Instruments, Winooski, VT), on AO-Green and AO-Red channels.

Image processing and analysis

A cellpose model was trained on images from Huh-7 cells stained with AO to identify the nuclei object using the cellpose GUI (Pachitariu and Stringer, 2022) (model available here https://github.com/broadinstitute/scripts_notebooks_fossa/tree/main/cellpose/Acridine_Orange_Model_Huh7). One image from every experiment was randomly selected to create the train and test. The models were used to segment the nuclei on all our analysis pipelines using the CellProfiler plugin RunCellpose that runs cellpose custom models (Weisbart et al., 2023). To segment cell boundaries, we used the AO-GFP channel, which highlights RNA staining in the cytoplasm, facilitating accurate segmentation using the propagation method implemented on CellProfiler. This method defines where the boundaries between objects are by a combination of proximity to the nearest primary object and variations in intensity gradients (see Supplemental Figures S17 and S19 for overlay examples). Then, a pipeline was created on CellProfiler version 4.2.5 to segment the nuclei, cells, cytoplasm, nucleoli, and vesicles, and an overlay of the segmented objects was created above the images to check for image segmentation (Carpenter et al., 2006; Stirling et al., 2021). The pipeline was run for one image of every well in every plate before running the analysis, to check for errors in object segmentation. An example pipeline is available here https://github.com/broadinstitute/scripts_notebooks_fossa/tree/main/cellprofiler/LiveCellPainting_pipeline.

After segmentation, features were extracted from the single-cell objects using CellProfiler modules. Features related to the area and shape of the objects were extracted, such as area, perimeter, and HuMoment (Hu,); the integrated, mean, and other features related to pixel intensity were measured in every channel and object (cell, nuclei, and cytoplasm); the degree and nature of textures in images and objects to quantify their roughness and smoothness (Haralick et al., 1973). The cells were segmented into four concentric rings going from the center of the cell to the border of the cell, and the total and mean intensity of the AO-Green and AO-Red was measured within each ring. The pipelines were run using a version of CellProfiler optimized to run inside Amazon Web Services, the Distributed-CellProfiler (Weisbart and Cimini, 2023). To join the CSV files generated per site, the pycytominer function collate from the “cyto utilities” package was used (Serrano et al., 2025).

Image visualization

Fluorescence images presented in this study were processed and visualized using the scikit-image Python library. Specifically, intensity normalization was performed using `skimage.exposure.rescale_intensity`, which adjusts pixel intensities to a standardized range for improved visualization. To ensure consistency, intensity scaling was applied uniformly across all images within a given figure, rather than independently for each image. This approach preserves relative intensity differences across conditions while allowing for meaningful visual comparisons. Images were not altered beyond intensity scaling, and no artificial enhancements were applied.

Profiling

To process the features and obtain a meaningful profile (Chandrasekaran et al., 2021), Pycytominer was used to process image-based profiles (Serrano et al., 2025). Profiles were ag-

gregated from single-cell to well-aggregated profiles using the median function from the Pycytominer function “aggregate.” Annotation was also performed with Pycytominer to add all relevant information for each data frame, such as compound name, the concentration used, cell type, etc. The features were normalized relative to the negative control on a per-plate basis to address batch effects using the RobustMAD function, which takes the feature value (x) minus the median divided by the median absolute value (scaled feature = $[x - \text{median}/\text{mad}]$). Feature selection was performed to exclude features that have more than 5% of NA values, features with low variance, features that correlate higher than 90%, and features that have values higher than 500 (outliers). Notebooks for profiling are available here https://github.com/broadinstitute/scripts_notebooks_fossa/tree/main/profiles/cellprofiler. Batch correction was applied to correct the effect of performing the experiment on different days. pyCombat (an implementation of ComBat in Python; example notebook is available here https://github.com/broadinstitute/scripts_notebooks_fossa/blob/main/pycombat_umap/apply_pycombat_visualize.ipynb) (Behdenna *et al.*, 2020) was used because of its characteristic of correcting for batch effect in small sample sizes. From here, when a profile is defined, we consider that all these steps were applied before analyzing the results.

Profile evaluation

The replicate retrieval ability was measured using mAP. It measures the ability of a replicate to retrieve other replicates without classifying the negative control as a replicate. A query is created to retrieve replicates or negative controls, and a rank order is created. From those, the area under the precision-recall curve is measured. More details are available in (Dijk *et al.*, 2024). The test was performed using the evalzoo/matric library available at <https://github.com/cytomining/evalzoo/tree/main/matric>.

To visualize the profiles in a dimensionality-reduced space, t-SNE (Maaten and Hinton, 2008) or UMAP (Uniform Manifold Approximation and Projection) (McInnes *et al.*, 2020) was used to generate the vectors for visualization. The embeddings were generated for 100 iterations, and the mean and SD embeddings were calculated and presented in the plots.

HDBSCAN was performed by following the example available at <https://umap-learn.readthedocs.io/en/latest/clustering.html>. UMAP is used for dimensionality reduction, and HDBSCAN is performed to predict the labels based only on the density of the points (an unsupervised clustering method).

Statistical analysis

Statistical analysis was performed to compare the negative control with each compound presented on every assay. The statannotations library was used for all the tests performed in this article (Charlier *et al.*, 2022). In the acidification inhibitors assay (Figure 2), an independent t test was used to test the total intensity differences between the negative control and acidification inhibitors. In the dose-response assay with AgNP (Figure 3), Mann–Whitney was used to test all concentrations of AgNP against the negative control. More details for each test can be found in the caption of each plot, but in general, the p value was displayed as *, $0.01 < p \leq 0.05$; **, $0.001 < p \leq 0.01$; ***, $0.0001 < p \leq 0.001$; and **** $p \leq 0.0001$. An example notebook is available here https://github.com/broadinstitute/scripts_notebooks_fossa/blob/main/individual_feature_and_statistics/Individual_Features_Statistics.ipynb.

DATA AVAILABILITY

Analysis notebooks and scripts are available at <https://github.com/fefossa/livecellpainting.git>

Images will be made available at <https://github.com/broadinstitute/cellpainting-gallery>.

ACKNOWLEDGMENTS

This work was supported by funds provided by São Paulo Research Foundation (FAPESP) #2022/01483-4, #2019/24033-1, #2023/06143-0 and #2020/01218-3. This work was also supported by funds provided by the National Institutes of Health (NIH COBA P41 GM135019 to B.A.C. and A.E.C. and MIRA R35 GM122547 to A.E.C.). This project has been made possible in part by grant number 2020-225720 (to B.A.C.) from the Chan Zuckerberg Initiative DAF, an advised fund of the Silicon Valley Community Foundation.

REFERENCES

- André O, Kumra Ahnlide J, Norlin N, Swaminathan V, Nordenfelt P (2023). Data-driven microscopy allows for automated context-specific acquisition of high-fidelity image data. *Cell Rep Methods* 3, 100419.
- Anthérieu S, Fromenty B, Robin MA, Guilloze A (2010). Amiodarone-induced phospholipidosis and steatosis in human hepatoma HepaRG cells. *Toxicol Lett* 196, S308–S209.
- Behdenna A, Haziza J, Azencott C-A, Nordor A (2020). pyComBat, a Python tool for batch effects correction in high-throughput molecular data using empirical Bayes methods. *bioRxiv*.
- Binó L, Mikulenková E, Štěpánek L, Bernatík O, Vysloužil D, Pejšková P, Gorilák P, Huranová M, Varga V, Čajánek L (2022). A protocol for generation and live-cell imaging analysis of primary cilia reporter cell lines. *STAR Protoc* 3, 101199.
- Bray M-A, Singh S, Han H, Davis CT, Borgeson B, Hartland C, Kost-Alimova M, Gustafsdottir SM, Gibson CC, Carpenter AE (2016). Cell painting, a high-content image-based assay for morphological profiling using multiplexed fluorescent dyes. *Nat Protoc* 11, 1757–1774.
- Carpenter AE, Jones TR, Lamprecht MR, Clarke C, Kang IH, Friman O, Guertin DA, Chang JH, Lindquist RA, Moffat J, *et al.* (2006). CellProfiler: Image analysis software for identifying and quantifying cell phenotypes. *Genome Biol* 7, R100.
- Chandrasekaran SN, Ceulemans H, Boyd JD, Carpenter AE (2021). Image-based profiling for drug discovery: Due for a machine-learning upgrade? *Nat Rev Drug Discov* 20, 145–159.
- Charlier F, Weber M, Izak D, Harkin E, Magnus M, Lalli J, Fresnais L, Chan M, Markov N, Amsalem O, *et al.* (2022). Statannotations (v0.6). Zenodo.
- Chen M, Suzuki A, Thakkar S, Yu K, Hu C, Tong W (2016). DILI-rank: The largest reference drug list ranked by the risk for developing drug-induced liver injury in humans. *Drug Discov Today* 21, 648–653.
- Cho MK, Seo MJ, Juvekar V, Jo JH, Kim W, Choi KS, Kim HM (2020). Screening of drug-induced steatosis and phospholipidosis using lipid droplet-selective two-photon probes. *Anal Chem* 92, 11223–11231.
- Cimini BA, Chandrasekaran SN, Kost-Alimova M, Miller L, Goodale A, Fritchman B, Byrne P, Garg S, Jamali N, Logan DJ, *et al.* (2023). Optimizing the cell painting assay for image-based profiling. *Nat Protoc* 18, 1981–2013.
- Cuny AP, Schlottmann FP, Ewald JC, Pelet S, Schmöller KM (2022). Live-cell microscopy: From image to insight. *Biophys Rev* 3, 021302.
- Dijk Rv, Arevalo J, Babadi M, Carpenter AE, Singh S (2024). Capturing cell heterogeneity in representations of cell populations for image-based profiling using contrastive learning. *PLoS Comput Biol* 20, e1012547.
- Donato MT, Tolosa L (2021). High-content screening for the detection of drug-induced oxidative stress in liver cells. *Antioxidants* 10, 106.
- Duong H, Bajaj T (2023). Lovastatin. Treasure Island (FL): StatPearls Publishing.
- Farhy C, Hariharan S, Ylanko J, Orozco L, Zeng F-Y, Pass I, Ugarte F, Forsberg EC, Huang C-T, Andrews DW, Terskikh AV (2019). Improving drug discovery using image-based multiparametric analysis of the epigenetic landscape. *ELife* 8, e49683.
- Florek JB, Lucas A, Girzadas D (2023). Amiodarone. Treasure Island (FL): StatPearls Publishing.
- García-Fossa F, Cruz MC, Haghighi M, de Jesus MB, Singh S, Carpenter AE, Cimini BA (2023). Interpreting image-based profiles using similarity clustering and single-cell visualization. *Curr Protoc* 3, e713.

- Garvey CM, Spiller E, Lindsay D, Chiang C-T, Choi NC, Agus DB, Mallick P, Foo J, Mumenthaler SM (2016). A high-content image-based method for quantitatively studying context-dependent cell population dynamics. *Sci Rep* 6, 29752.
- Gordonov S, Hwang MK, Wells A, Gertler FB, Lauffenburger DA, Bathe M (2016). Time series modeling of live-cell shape dynamics for image-based phenotypic profiling. *Integr Biol* 8, 73–90.
- Ha S-W, Neale Weitzmann M, Beck GR (2014). Bioactive silica nanoparticles promote osteoblast differentiation through stimulation of autophagy and direct association with LC3 and p62. *ACS Nano* 8, 5898–5910.
- Haralick RM, Shanmugam K, Dinstein I (1973). Textural features for image classification. *IEEE Trans Syst Man Cybern SMC-3*, 610–621.
- Henry WS, Laszewski T, Tsang T, Beca F, Beck AH, McAllister SS, Tokar A (2017). Aspirin suppresses growth in PI3K-mutant breast cancer by activating AMPK and inhibiting mTORC1 signaling. *Cancer Res* 77, 790–801.
- Homewood CA, Warhurst DC, Peters W, Baggaley VC (1972). Lysosomes, pH and the anti-malarial action of chloroquine. *Nature* 235, 50–52.
- Huang S, Dai R, Zhang Z, Zhang H, Zhang M, Li Z, Zhao K, Xiong W, Cheng S, Wang B, Wan Y (2023). CRISPR/Cas-based techniques for live-cell imaging and bioanalysis. *Int J Mol Sci* 24, 13447.
- Kalinin AA, Arevalo J, Vulliard L, Serrano E, Tsang H, Bornholdt M, Rajwa B, Carpenter AE, Way GP, Singh S (2024). A versatile information retrieval framework for evaluating profile strength and similarity. *bioRxiv*.
- Kornhuber J, Parsons CG, Hartmann S, Retz W, Kamolz S, Thome J, Riederer P (1995). Orphenadrine is an uncompetitive N-methyl-D-aspartate (NMDA) receptor antagonist: Binding and patch clamp studies. *J Neural Transm Gen Sect* 102, 237–246.
- Lazar NH, Celik S, Chen L, Fay MM, Irish JC, Jensen J, Tillinghast CA, Urbanik J, Bone WP, Gibson CC, Haque IS (2024). High-resolution genome-wide mapping of chromosome-arm-scale truncations induced by CRISPR-Cas9 editing. *Nat Genet* 56, 1482–1493.
- Li S, Xia M (2019). Review of high-content screening applications in toxicology. *Arch Toxicol* 93, 3387–3396.
- Lin S, Schorpp K, Rothenaigner I, Hadian K (2020). Image-based high-content screening in drug discovery. *Drug Discov Today* 25, 1348–1361.
- Maaten Lvd, Hinton G (2008). Visualizing data using t-SNE. *J Mach Learn Res* 9, 2579–2605.
- McInnes L, Healy J, Melville J (2020). UMAP: Uniform manifold approximation and projection for dimension reduction. *J Open Source Softw* 3, 861.
- Montecucco A, Zanetta F, Biamonti G (2015). Molecular mechanisms of etoposide. *EXCLI J* 14, 95–108.
- Nakashima A, Higashisaka K, Kusabiraki T, Aoki A, Ushijima A, Ono Y, Tsuda S, Shima T, Yoshino O, Nagano K, *et al.* (2019). Autophagy is a new protective mechanism against the cytotoxicity of platinum nanoparticles in human trophoblasts. *Sci Rep* 9, 5478.
- Ogino MH, Tadi P (2023). Cyclophosphamide. Treasure Island (FL): StatPearls Publishing.
- Pachitariu M, Stringer C (2022). Cellpose 2.0: How to train your own model. *Nat Methods* 19, 1634–1641.
- Pierzyńska-Mach A, Janowski PA, Dobrucki JW (2014). Evaluation of acridine orange, LysoTracker Red, and quinacrine as fluorescent probes for long-term tracking of acidic vesicles. *Cytometry A* 85, 729–737.
- Rumore MM, Schlichting DA (1985). Analgesic effects of antihistaminics. *Life Sci* 36, 403–416.
- Schnell U, Dijk F, Sjollem KA, Giepmans BNG (2012). Immunolabeling artifacts and the need for live-cell imaging. *Nat Methods* 9, 152–158.
- Wang W, Douglas D, Zhang J, Kumari S, Selase Enuameh M, Dai Y, Wallace CT, Watkins SC, Shu W, Xing J (2020). Live-cell imaging and analysis reveal cell phenotypic transition dynamics inherently missing in snapshot data. *Sci Adv* 6, eaba9319.
- Serrano E, Chandrasekaran SN, Bunten D, Brewer KI, Tomkinson J, Kern R, Bornholdt M, Fleming S, Pei R, Arevalo J, *et al.* (2025). Reproducible image-based profiling with Pycytominer. *Nat Methods* 22, 677–680.
- Siegmund D, Fassler M, Heyse S, Steigele S (2022). Benchmarking feature selection methods for compressing image information in high-content screening. *SLAS Technol* 27, 85–93.
- Stirling DR, Swain-Bowden MJ, Lucas AM, Carpenter AE, Cimini BA, Goodman A (2021). CellProfiler 4: Improvements in speed, utility and usability. *BMC Bioinformatics* 22, 433.
- Thomé MP, Filippi-Chiela EC, Villodre ES, Migliavaca CB, Onzi GR, Felipe KB, Lenz G (2016). Ratiometric analysis of acridine orange staining in the study of acidic organelles and autophagy. *J Cell Sci* 129, 4622–4632.
- Tolosa L, Jiménez N, Pelechá M, Castell JV, Gómez-Lechón MJ, Donato MT (2019). Long-term and mechanistic evaluation of drug-induced liver injury in Upcyte human hepatocytes. *Arch Toxicol* 93, 519–532.
- Watson ER, Taherian Fard A, Mar JC (2022). Computational methods for single-cell imaging and omics data integration. *Front Mol Biosci* 8, 768106.
- Way GP, Sailem H, Shave S, Kasprovicz R, Carragher NO (2023). Evolution and impact of high-content imaging. *SLAS Discov* 28, 292–305.
- Way GP, Spitzer H, Burnham P, Raj A, Theis F, Singh S, Carpenter AE (2022). Image-based profiling: A powerful and challenging new data type. *Pac Symp Biocomput* 27, 407–411.
- Weisbart E, Cimini BA (2023). Distributed-Something: Scripts to leverage AWS storage and computing for distributed workflows at scale. *Nat Methods* 20, 1120–1121.
- Weisbart E, Tromans-Coia C, Diaz-Rohrer B, Stirling DR, Garcia-Fossa F, Senft RA, Hiner MC, de Jesus MB, Eliceiri KW, Cimini BA (2023). CellProfiler plugins—An easy image analysis platform integration for containers and Python tools. *J Microsc* 296, 227–234.
- Yang G, Wang Y, Feng J, Liu Y, Wang T, Zhao M, Ye L, Zhang X (2017). Aspirin suppresses the abnormal lipid metabolism in liver cancer cells via disrupting an NF- κ B-ACSL1 signaling. *Biochem Biophys Res Commun* 486, 827–832.
- Yoshimori T, Yamamoto A, Moriyama Y, Futai M, Tashiro Y (1991). Bafilomycin A1, a specific inhibitor of vacuolar-type H(+)-ATPase, inhibits acidification and protein degradation in lysosomes of cultured cells. *J Biol Chem* 266, 17707–17712.
- Zanella F, Lorens JB, Link W (2010). High-content screening: Seeing is believing. *Trends Biotechnol* 28, 237–245.